



Characterizing devolatilized wood pellets for fluidized bed applications

Kolja Jarolin¹ · Shen Wang² · Timo Dymala¹ · Tao Song³ · Stefan Heinrich¹ · Laihong Shen² · Maksym Dosta¹

Received: 28 January 2021 / Revised: 29 March 2021 / Accepted: 29 March 2021
© The Author(s) 2021

Abstract

We investigated devolatilized wood pellets to characterize their mechanical behavior and their microstructure. The work's aim is to increase the understanding and modeling capabilities for the application in fluidized bed gasification as a sustainable alternative to generate synthesis gas. Our experiments showed that devolatilized wood pellets are a stable but highly porous and fragile structure. Computed tomographic images of the same pellets before and after devolatilization showed that the existing pore network in raw conditions characterizes the final structure. Along with the pores, the reaction rate likely increases and the pores massively enlarge, and internal cavities are formed. The resulting pore network dominates the mechanical behavior and leads to micro fragmentations already at low static loads or slow dynamic impacts. This results in the creation of fines or breakage already at low impact velocities. For fluidized bed devolatilization, the large-scale open pore network of the biochar pellets allows the penetration of bed material into the pellet leading to an estimated increase in the pellet's mass of up to 45%. However, an increase in pore size caused by the penetration was not apparent. Due to the pellet's porous structure, breakage and attrition induced by mechanical stresses are likely to be as or even more important than primary fragmentation caused by the devolatilization process itself in a reactor.

Keywords Mechanical characterization · Wood pellets · Devolatilization · Gasification · Micro computed tomography · Mechanical strength · Attrition

1 Introduction

To reduce greenhouse gas emissions and mitigate climate change, alternatives to the usage of natural gas are needed. Gasification of biomass might be one possible approach, to generate synthesis gas from biomass and replace natural gas sustainably and effectively for some applications. To achieve better fuel properties, pelletized biomass can be used [1, 27]. Biomass pellets are heterogeneous materials

made from dry biomass powder in a pressure-assisted densification process [32]. For example, wood pellets are typically based on dry untreated wood that is hammermilled into sawdust and chipped wood. Mechanical densification in standard process conditions enables a reduction of transport and storage costs of the product [26]. Furthermore, uniformity in water content, chemical composition, and form as well as high product density and high heating value of 19 GJ/t enable the usage of pellets in form of solid biofuels for energy and heat production in industrial-sized heat and production plants [12, 13, 17].

By gasification, biomass pellets can be converted to environmental-friendly synthesis gas. Synthesis gas or syngas consists mainly of carbon monoxide, hydrogen, methane, and carbon dioxide [20]. Gasification is a thermo-chemical conversion process typically operated at temperatures higher than 650 °C. In general, it is an endothermic process converting the fuel into a gaseous and solid phase, called char. Char consists of ash and unconverted carbon, which amounts depend on the process. The energy required is typically supplied by partially oxidizing the fuel. Effectively, the conversion of biomass

✉ Kolja Jarolin
kolja.jarolin@tuhh.de

¹ Institute of Solids Process Engineering and Particle Technology, Hamburg University of Technology, TUHH, Denickestr. 15, 21073 Hamburg, Germany

² Key Laboratory of Energy Thermal Conversion and Control of Ministry of Education, Southeast University, Nanjing 210096, China

³ School of Energy and Mechanical Engineering, Nanjing Normal University, Nanjing 210023, China

into syngas increases the heating value and allows a more widespread usage of the biomass.

A complex set of more than a hundred different reactions are involved in the conversion which is in general carried out in presence of a gasifying agent [6, 9, 14]. To achieve high efficiency of the process, fluidized bed reactors can be used [14]. Their high mixing and gas-solid contact enable high carbon conversion rates. Especially the conversion of tars (heavier hydro-carbons) into basic components can be increased. Different process concepts are investigated to further improve the technology and optimize efficiency [5, 7, 18, 35].

A common problem of all approaches using fluidized bed reactors is the increased attrition and breakage of the material inside the reactor [22, 31]. This also includes the biomass fuel pellets. Attrition and breakage of the pellets can impact the process performance due to fines leaving the reactor unreacted or due to a change of the reactor dynamics caused by the changed solid size distribution. For example, [1] found that in their lab-scale fluidized bed plant, about 25% of the fixed carbon biomass was elutriated unreacted.

In fluidized bed conversion, multiple phenomena can lead to attrition and fragmentation. Following the categorization by [22], there are four phenomena relevant for attrition of solid fuels. Firstly, there is primary fragmentation due to thermal shocks or induced by the chemical reaction. Secondly, secondary fragmentation occurs due to impacts. Thirdly, attrition by abrasion is involved and fourthly, there is percolative fragmentation due to the loss of connectivity of porous particles. These four phenomena cause a significant change in the reactor dynamics [22]. Therefore, for fully understanding the processes and enable efficient modeling and scaling, a sufficient understanding of the breakage and attrition behavior is necessary. For this purpose, the work at hand studies the modification in the mechanical properties of devolatilized wood pellets. Wood pellets were chosen as an example for their broad usage and availability. Devolatilization, which corresponds to the pyrolysis reaction, is the primary process that is changing the pellet in a reactor since biomass consists mainly of volatiles (70–90 wt%). The remaining solid phase primarily consists of a fixed carbon and a small ash content. The fixed carbon can also be converted into syngas in a much slower reduction reaction, or it can, for example, be oxidized by transporting it to another reactor (see, e.g., [23]).

For the properties of raw wooden pellets, many studies already exist [4, 11, 15, 25, 26]. Related to the properties during and after thermo-chemical conversion only some aspects can already be found in the literature. Paulauskas et al. [16] studied shrinkage and swelling during pyrolysis of wood pellets. Strandberg et al. [28] showed with computed tomography images the generation

of cavities during devolatilization and the change in the structure during combustion. With our work, we want to extend the available literature with a systematic analysis of relevant properties for fluidized bed reactors and how they interact. We are focusing this investigation on understanding the general behavior and breakage. Namely, the structural changes, the static breaking strength, and the impact resistance are primarily examined. Therefore, the work at hand gives new insights into how char pellets behave under static and dynamic loads and how this relates to the pellet's structure. For fluidized bed operations, this is mainly relevant for accounting for changes in the particle size distribution and in the fluid dynamics.

2 Methods and materials

In the following, the different types of wood pellets will be introduced, and the different utilized methods for devolatilization are explained. Afterward, the methods for analysis are described. Besides some basic descriptive parameters, the uni-axial compression testing and the dynamic impact testing as well as image analysis based on micro computed tomography will be described.

2.1 Wood pellets

As a natural product, the properties of wood pellets fluctuate. This includes the composition as well as the mechanical properties. For example, the strength and durability of densified materials are affected by many factors, such as age and storage conditions of the raw material, moisture content, processing conditions (pressure and temperature, binder, feedstock mixture) and, especially, they depend on the strength of the binding forces holding the individual particles together [12, 26, 33]. The binding forces can be classified into five major groups: solid bridges, mechanical interlocking forces, attraction forces between solid particles, adhesion and cohesion forces, and interfacial forces and capillary pressure [4, 10, 21].

In the case of the wood pellets, lignin contained in the feed material acts as a binder and provides the product's high durability. During the densification process at elevated temperature, lignin, which is one of the main components of the wood, softens and fills the pores between wood chips. Thereby, the lignin matrix of the pellet, where the wood particles are embedded in, is generated. Larger particles present structural weak points, which cause cracks and material fracture. Finer grinding results in a denser and more homogeneous structure and greater durability.

Thus, it is not possible to describe wood pellets as a whole. To get, nevertheless, a wider understanding three different types of wood pellets are used in this work:

Fig. 1 Images of the used pellets in the raw state

Type A: is a white sawdust pellet from spruce wood and a mean diameter of 6 mm from the company PowerPellets Vertriebs GmbH & Co. KG (Germany);

Type B: is a brown sawdust pellet from foliage and coniferous wood with a 6-mm diameter from the company Plospan Bio-Energy B.V. (Netherlands);

Type C: is a brown sawdust pellet from mixed, unspecified wood types with a 9-mm diameter from the company Dingliang Co. (China).

All three types of wood pellets are commercially available pellets. Photos of all types are shown in Fig. 1. In the work at hand, we will use the Type A pellet as a basis and countercheck the results with measurements of the other types of pellets. The pellets of Type A and Type B were studied at the Hamburg University of Technology (TUHH), Germany. The pellets of Type C were mainly studied at the Nanjing Normal University and Southeast University, China.

For all types, a proximate analysis and an ultimate analysis are performed. All ultimate analyses were conducted by the central laboratory of the TUHH. The proximate analysis is based on DIN 51734 [3]. The results are shown in Table 1. The general composition of all types is very similar. Only the Type C pellets have slightly less volatiles and more nitrogen.

2.2 Sample preparation

Since many of the measured properties, like the mechanical strength, strongly depend on the dimensions of the analyzed pellets, the lengths of the investigated pellets have been adjusted by a grinding and cutting process. Almost for all tests, except impact tests, pellets with a length of 10 mm were analyzed. Besides the definition of the length, the

cutting allows us to obtain relatively smooth cut surfaces and, hence, reduces the fluctuations of the results. After cutting, the pellets are devolatilized with three different processes to get a broad understanding of the behavior of devolatilized pellets:

A *Muffle furnace* (MF) is used to represent the baseline with slow heating and no gas flow.

Heated tube reactors with a very low gas flow (LFR) or with high, preheated gas flow (HFR) are used. This treatment increases the heat flux strongly but still does not induce any additional mechanical stresses.

Fluidized bed reactors (FBR) with quartz sand as bed material and operated as a bubbling bed is used as the third type. Compared to the two previous methods, the bubbling bed will increase the heat flux experienced by the pellet further but also induce damages during the sample preparation.

In all devolatilization methods, the reactor temperature is kept at 900 °C. The details about the different methods will be explained in the following sections.

2.2.1 MF—muffle furnace

As a baseline, all types of pellets were devolatilized in closed crucibles in a muffle furnace. The furnace Heraeus MR 170 E was used for all experiments. The process for devolatilization was developed based on the DIN 51720 [2] describing the quantification of the volatile matter of solid fuels. Hence, in the first step, the quartz crucibles are burned empty. Afterward, they are cooled down to room conditions and filled with one pellet. The closed crucibles are then inserted into the muffle furnace at 900 °C and kept there for

Table 1 For all three types of wood pellets used, the proximate analysis with values shown as received (ar) and the ultimate analysis with values shown on water free basis (wf) is given

	Approx. diameter [mm]	Moisture (ar) [wt%]	Ash (ar) [wt%]	Volatile matter (ar) [wt%]	N (wf) [g/kg]	C (wf) [g/kg]	H (wf) [g/kg]	S (wf) [g/kg]
Type A	6	7.8	0.2	77	<1.00	471	65.0	<2.00
Type B	6	7.2	0.3	75	2.15	479	63.4	<2.00
Type C	9	6.2	3.8	73	6.35	460	60.8	<2.00

7 min. Finally, the closed crucibles are cooled down to room temperatures again.

2.2.2 FBR—fluidized bed reactor for Type A and Type B pellets

The fluidized bed reactor for Type A and B pellets consists of a pipe with an inner diameter of 53 mm. The pipe is heated by an electrical heating system. The gas flow is preheated by routing it through the electrical heating before entering the reactor tube. A schematic drawing of the plant is shown in Fig. 2.

More details about the reactor can be found in [8]. The biomass pellets are fed through a small pipe ending shortly before the distributor plate. Before feeding, the pellets are kept outside the reactor in a closed plastic hose connected to the pipe. This allows feeding one pellet at a time without preheating the pellet. To extract the pellets from the reactor a basket is inserted into the reactor. The diameter of the basket is slightly smaller than the inner diameter of the reactor and it is built from a steel mesh with a grid size bigger than the maximal bed material size. Hence, it allows the bed material to pass through the mesh.

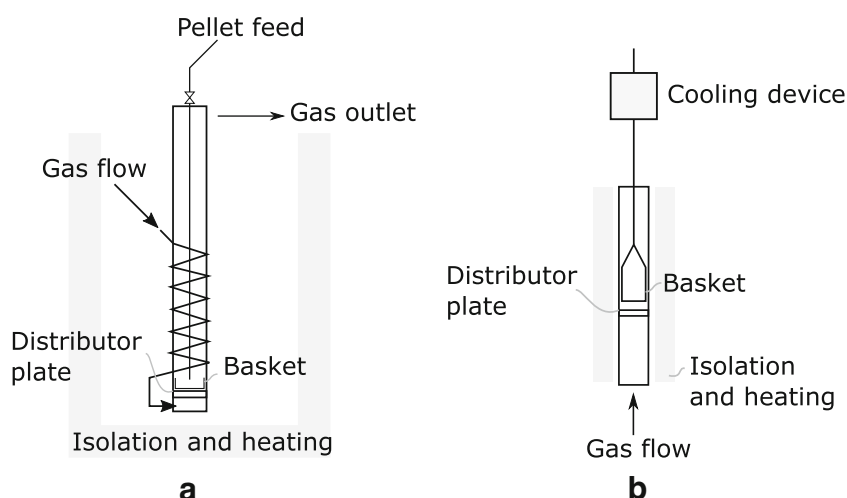
For all fluidized bed experiments with this reactor, 90 g quartz sand is used as bed material. The mean diameter of the sand is about 200 μm . See [34] for a detailed analysis of the used bed material. The bed is fluidized with nitrogen with a volume flow of 2.5 l/min. The bed is heated to 900 $^{\circ}\text{C}$ before inserting the first pellet. Assuming an isobaric expansion of an ideal gas from 20 $^{\circ}\text{C}$ to 900 $^{\circ}\text{C}$ the volume flow results in a superficial gas velocity of approximately 8 cm/s. Using the correlation proposed by [30], the superficial gas velocity can be estimated to be approximately about 4 times the estimated minimum fluidization velocity.

Pellets are fed consecutively, ensuring that no significant amount of syngas is present before the next pellet is fed. Thus, the residence time in the reactor is different for each pellet. Since no reaction is taking place after the devolatilization, this will only increase the time the pellets are exposed to the mechanical load in the fluidized bed. To reduce the possible influence due to different residence times and reactor conditions, a maximum of 30 g raw biomass is fed, resulting in roughly 30 min of operation. Afterward, the reactor is slowly cooled down. For the first two hours of cooling, the bed is still fluidized. We chose to fluidize the bed during cooling because cooling the pellets in a fixed bed would result in an untypical mechanical load for the pellets, and more bed material would get stuck on the surfaces of the pellets. The extraction of the pellets during the operation was technically not possible. As a side effect, the continuation of the fluidization causes the different residence time of the pellets during operation to, likely, become neglectable. After cooling the basket is removed from the reactor.

2.2.3 HFR—heated tube reactor with high flow for Type A and Type B

As high gas flow reactor for Type A and B pellets, the fluidized bed reactor of the last section is used. The goal of the operation condition is to achieve fast heating but avoid pre-damaging the pellets. Therefore, the reactor is operated without bed material. However, the volume flow of nitrogen is kept constant leading also to a gas velocity of approximately 8 cm/s. Since the gas is preheated, a high convective heat transfer can still be realized. The pellets are fed again consecutively until a maximum of 30 g raw biomass is reached, and the reactor is cooled down. The amount of raw biomass fed to the reactor is limited to improve the similarity of the conditions for all pellets.

Fig. 2 Schematic drawings of the used fluidized bed apparatuses. **a** Fluidized bed reactor (FBR) and high flow reactor (HFR) for Type A and Type B pellets. **b** Fluidized bed reactor (FBR) and low flow reactor (LFR) for Type C pellets



2.2.4 FBR—fluidized bed reactor for Type C

The fluidized bed reactor used for devolatilization of the pellets of Type C consists of a pipe with a uniform inner diameter of 32 mm. A schematic representation is also shown in Fig. 2. In this reactor, pellet feeding and extraction can be achieved continuously by a moveable basket. The basket consists of a mesh with a mesh size bigger than the bed material. The pellet in the basket can be actively cooled after removing it. In contrast to the other fluidized bed reactor, the fluidization gas is not preheated, but the distributor plate is fixed at a high position to achieve a hot fluidization gas stream. As bed material, also quartz sand is used, but the mean diameter is slightly higher with 375 μm . The bed is fluidized with nitrogen with a volume flow of 2.0 l/min. Based on the assumption of an ideal gas, the superficial gas velocity at the reactor temperature of 900 °C can be calculated to be approximately 16 cm/s. Therefore, the gas velocity is roughly three times the estimated minimum fluidization velocity. Hence, the flow regime is expected to be very similar to the other fluidized bed reactor.

2.2.5 LFR—heated tube reactor with low flow for Type C

The reactor described above is also used to generate non-damaged devolatilized pellets. A gas flow of 0.1 l/min without any bed material is used in the process. The reactor is kept again at 900 °C. Based on the assumption of an ideal gas the gas velocity can be calculated to be approximately 0.3 cm/s. The surrounding condition will result in a heating rate between the muffle furnace and the high gas flow reactor for Type A and Type B pellets.

2.3 Basic descriptive parameters

For describing the fundamental changes of the wood pellets during devolatilization, two simple and easy to measure metrics will be used: the apparent density and the apparent volume scaling factor. Both variables are called apparent because they are based on the apparent volume. The apparent volume (V_{app}) is the volume of an enclosing convex surface including all internal pores. We will only be estimating the values and assume the pellet has a cylindrical shape before and after devolatilization. The error of this estimation for devolatilized pellets will be discussed in Section 3 about the results of the micro computed tomography imaging.

The apparent density (ρ_{app}) is especially interesting for modeling the fluid dynamics of a reactor system. It is simply calculated by:

$$\rho_{\text{app}} = \frac{m_{\text{pellet}}}{V_{\text{app}}} = \frac{m_{\text{pellet}}}{\pi l R_p^2} \left[\frac{\text{kg}}{\text{m}^3} \right], \quad (1)$$

where m_{pellet} [kg] is the measured mass and R_p [m] and l [m] are the pellet's radius and length, respectively. Since the pellets have an almost flat surface after cutting and grinding, the length is measured with a caliper. The pellet's radius is measured with a caliper or by the compression tester, where the pellet is compressed with a moving flat punch. Based on the analysis of the force-displacement characteristic, the first contact point with significant force can be detected and is used as well to estimate the pellet radius. Both methods are combined to get an approximation of the average radius.

To quantify the change in volume during devolatilization, volume scaling factors are calculated. The factor is defined by the quotient of the volume after devolatilization and the initial pellet's volume. We will use the apparent values for calculating the factor and, thus, refer to them as apparent volume scaling factors. To analyze the anisotropy of the shrinkage, the scaling factors for the diameter and the length of pellet are also calculated.

2.4 Uni-axial compression test

For characterizing the mechanical strength, uni-axial compression tests are carried out in the radial direction. The goal is to approximate a quasi-static loading scenario. Therefore, a very low loading speed of the compressing stamp is applied. In the case of pellets of Type A and Type B the velocity is equal to 0.1 mm/s and for the pellets of Type C it is equal to 0.167 mm/s. The pellets are analyzed either with a TA.XT Texture Analyzer (Stable Micro Systems Ltd, UK) or with a Digital Push-Pull Gauge (HP-500, Handpi Co., China). From the tests, force-displacement curves are obtained.

To compare the mechanical strength we are using the breakage energy per unit mass at the given point. For this purpose, the force-displacement curve is integrated and divided by the average pellet mass in the devolatilized state of the given type and length.

Note that even in the raw state, the strength of the pellet is very different. This can, for example, be seen by comparing the elastic proportionality limit for the pellets in raw conditions. The proportionality limit is the point, where the force-displacement graph levels off and the graph is not straight anymore. The point corresponds roughly to the yield point. The proportionality limits are shown in Table 2. They were all measured with a Series 1600 Universal Testing Machine (Applied Test Systems, USA), allowing much higher forces than the previously mentioned devices. For comparison, the explained transformation to the breakage energy is conducted for the mean values and also shown in the table. The table's purpose is to illustrate the large variation in the pellet's strength. More measurements would be necessary to quantify the mean yield strength and the corresponding energy precisely.

Table 2 Measured mean proportionality limit and corresponding energy per unit mass for all pellet types in raw conditions with an approximate length of 10 mm to illustrate variations in raw conditions

Pellet type	Mean measured proportionality limit [N] (\pm standard deviation)	Estimated energy per unit mass at proportionality limit [J/kg]
Type A	334 (± 81)	≈ 270
Type B	170 (± 73)	≈ 80
Type C	335 (± 194)	≈ 125

2.5 Dynamic impact tests

To characterize the attrition behavior of the pellets, free-fall impact tests are conducted. The aim of this testing is to simulate in a controlled environment the impact of pellets at a specific velocity. To reduce the influence by different impact orientations, the pellets are started only in the axial direction. The pellet is accelerated by gravity and the impact velocity is only adjusted and controlled by the travel length.

At first, pre-tests with high impact velocities were conducted. The goal for the pre-test was to ensure a proper study design for the low velocity impacts, which are more likely to occur in a reactor and give more insights about the attrition by secondary fragmentation. Hence, by means of the pre-test, we wanted to obtain the approximate dimensions of breakage and abrasion caused by impacts. Therefore, the travel length was chosen to be 1.3 m. The velocity of the impact was estimated by the drop height. For the chosen height, air resistance has a slight influence and was, therefore, neglected. The impact velocity can be estimated to be around 4.5 m/s. The pre-tests showed that devolatilized pellets can withstand consecutive impacts. For example, to break Type C pellets devolatilized in the FBR between two and five consecutive drops were necessary. In contrast, some of the Type A pellets devolatilized in the MF could withstand more than 10 impacts. Hence, consecutive impacts lead to constant damaging. Thus, to study low impact velocity abrasion and breakage, a high amount of consecutive impacts is necessary and a high number of samples is necessary because of the large fluctuation.

Due to the pre-test results, the dynamic impact study was conducted with each pellet undergoing 100 consecutive impacts. After every ten impacts, the mass loss is measured with a high-precision scale. By this means, the continuous wear in a reactor of the pellet shall be estimated. Furthermore, the continuous damage may eventually lead to the breakage of the pellet. The breakage is characterized by fragmentation and the generation of fines. Typically, exactly two fragments exist. The fragments still consist of multiple bonded particles, and the cylindrical shape is typically still

visible. To ensure a strict separation between breakage and abrasion, we consider the pellet as broken if there are two segments with a shadow area in the magnitude of the initial cylinder's end face. Hence, the fragments will have a significant drag. If the pellet is considered broken, the test is stopped.

Due to the high scattering, mainly Type A pellets were tested. For Type A pellets, three different drop heights (2.5, 5.5, and 11.5 cm) and three different pellet lengths (1, 1.5, and 2 cm) are studied. In total, 75 different samples were prepared and tested in a randomized experimental plan. The velocity of the impact is calculated by the drop height y_0 [m]. For the used small heights, the air resistance can be neglected, and the velocity of the pellet at impact v [$\frac{m}{s}$] is estimated using the gravitational acceleration g [$\frac{m}{s^2}$]:

$$v = \sqrt{\frac{2y_0}{g}}. \quad (2)$$

Thus, the studied impact velocities are approximately 0.7, 1, and 1.5 m/s. The kinetic energy of the pellet at impact is estimated by

$$E_{\text{kin}} = 0.5m_{\text{pellet}}v^2. \quad (3)$$

The kinetic energy is used to get a single parameter describing both influencing variables. Two values will be evaluated in the work at hand, the breakage probability and the mass loss per impact. The breakage probability is calculated by the number of broken pellets divided by the total amount of pellets. The mass loss per impact is calculated by dividing the mass loss for each pellet (without breakage) by the number of impacts. The value will be normalized to the initial mass before the impact test.

To check how the behavior changes for different types of pellets, also 15 Type B pellets with a length of 1 cm and a drop height of 5.5 cm were tested.

2.6 Micro computed tomography characterization

To analyze the modification of the internal structure of the pellets, X-ray micro computed tomography (microCT) images were generated. We studied the change on basis of the pellets of Type A. For the analysis, the same pellet was imaged before and after devolatilization. MF and FBR devolatilization were applied to represent a large difference in the condition. To ensure that the orientation of the pellet can be identified between the images, one of the ends of the pellet was ground into an angle. To check the reproducibility of the data, an additional pellet was imaged each time and compared qualitatively to the main image. Furthermore, for comparison, a pellet devolatilized in the HFR was imaged.

All images were generated with the same device and settings. We used the Scanco μ CT 35 which is an X-ray

cone-beam microCT. A beam current of 177 μA and a peak voltage of 45000 V with a sample time of 2.4 s was used. The voxel size was set to 12 μm allowing efficient imaging of the entire pellet. All methods and concepts used for analyzing the resulting images are explained in the following.

2.6.1 Image recognition

For the one-to-one comparison of the microCT images, the orientation of the pellets must be fixed. At first, we transformed the image of the raw pellet such that the axial direction of the pellet corresponds to the z-axis and the face normal of the angled surface points towards the y-axis. Rotating to this specific orientation is not necessary but simplifies the analysis. The transformation and feature recognition were done in MATLAB R2019b. Firstly, the image was converted to a binary image, and the external surface was extracted into a point cloud. By using MATLAB's *pcfitcylinder* and *pcfitplane*, the necessary transformation was calculated and applied to the initial image. The same steps were applied on the images of the devolatilized pellets for a first approximate match of the orientation. Afterward, the *image recognition tool* from the AVIZO 2019.03 package was used to optimize the transformation of the image of the devolatilized pellet. The image recognition tool was also used later to calculate the difference in scale due to the devolatilization. As the final step, AVIZO's anisotropic diffusion filter was applied with a small diffusion stop threshold to reduce the noise in the image slightly.

2.6.2 Binarization and porosity analysis

To quantify the pore and pellet volume, the image must be binarized. Firstly, the convex outer surface was identified. For this purpose, mainly the following steps were applied in Avizo: Anisotropic diffusion with a high threshold, segmentation by threshold, manual modification in the segmentation editor, and spherical closing. The spherical closing is necessary since the pore network is open. Especially for the devolatilized pellets, there is no clear definition of where the pellet's outer surface is located. Therefore, the smallest sphere diameter closing all pores was used. We will call the resulting outer surface body-fitted surface. For identifying the pores inside the pellet, Avizo's porosities analysis wizard was used. For the given resolution and signal to noise ratio, an uncertainty for the thresholds exists. Therefore, different thresholds were used to represent a spectrum of visually acceptable binarizations. For reference, the 75% quantile of the linear attenuation coefficients representing pores in the image was about 0.08 for the used devolatilized pellet and microCT settings.

2.6.3 Pore size quantification

The final step for analyzing the pore network is to calculate a parameter describing the pore size. Typically, an equivalent pore diameter distribution is used (see, e.g., [36]). To calculate a pore diameter, a segmentation of the pore network in distinct pores and ducts is necessary. However, for the pellets, especially in the devolatilized state, no distinct pores exist. Instead, the pores are a complex three-dimensional interconnected network of voids. Therefore, a different parameter is used to compare the pore sizes between different images; the chord length distribution.

The chord is a straight line whose endpoints both lie on the boundary of the pore. It, therefore, depends on the chosen cutting plane. To get a representable variable for the pore size we are calculating the chord lengths for each row or column of pixels. Hence, summing all chord lengths results in the pore volume (in pixels). Furthermore, the three orthogonal planes defined by the normal of the coordinate space will be used as cutting plane. Due to the transformation of the pellet, they represent the chord lengths in axial direction of the pellet as well as two samples of the chord lengths in radial direction.

To get the distribution, the chord length values for each plane is partitioned into bins according to their pixel length. In the next step, the bins are weighted such that their values represent the volume fraction. For this purpose, the number of chords is multiplied by the chord length and divided by the total pellets volume as defined by the body-fitted surface described above:

$$F_i = n_i \cdot \frac{l_{\text{chord}}}{V_{\text{body-fitted}}}, \quad (4)$$

where F_i is the unitless bin's value, and l_{chord} the characteristic length of the chord in voxels, n_i the amount of chords with the given length l_{chord} and $V_{\text{body-fitted}}$ the total pellets volume in voxels. Based on the chosen microCT settings, 1 voxel corresponds to a volume of 12 μm^3 . Hence, F_i represents the volume occupied by all chords with the length l_{chord} . The sum over all bins is equal to the pellet's porosity.

Afterward, the bins for the three different cutting planes are averaged. The purpose is to achieve single values, which are insensitive to the chord's orientation and, at the same time, still sum-up to the total pore volume. For plotting the distribution, the chord lengths are multiplied by the voxel size to transform it to physical dimensions.

3 Results and discussion

In this section, we want to show with our results how devolatilization changes the behavior of the wood pellets.

Table 3 Apparent properties of the different pellet types and devolatilization methods

Devol. method	Pellet type	Apparent raw density	Apparent devol. density	Apparent volume scaling factor	Apparent axial scaling factor	Apparent radial scaling factor
		[kg/m ³]	[kg/m ³]	[%]	[%]	[%]
MF	A	1184 (±51)	434 (±35)	41 (±3)	77 (±2)	73 (±2)
MF	B	1056 (±33)	427 (±27)	42 (±4)	79 (±3)	73 (±3)
MF	C	1088 (±74)	449 (±40)	45 (±2)	82 (±1)	74 (±1)
LFR	C	1088 (±74)	392 (±10)	57 (±2)	91 (±1)	79 (±3)
HFR	A	1184 (±51)	289 (±15)	58 (±4)	84 (±3)	83 (±3)
HFR	B	1056 (±33)	260 (±13)	67 (±3)	86 (±2)	89 (±2)
FBR	A	1184 (±51)	290 (±20)	65 (±10)	85 (±4)	86 (±4)

(± standard deviation)

Firstly, the general structural changes are described on basis of the microCT imaging as well as the apparent density and volume. A general phenomenological model of the change in the internal structure will be derived and the influence of the different devolatilization methods will be discussed. In the second step, the pellets are characterized mechanically. For this purpose, the results of the uni-axial compression tests and the impact tests will be shown.

3.1 Structural changes

In general, the devolatilization of wood pellets leads to an overall shrinkage, an increase in porosity, and a decrease in density. All measured values for the used samples and methods are given in Table 3. The table shows that the magnitude of the measure depends mainly on the method of devolatilization. The values for the different types of pellets are relatively similar for each method and the differences between the methods are large. For example, the apparent density of Type A pellets devolatilized in the MF is about 50% higher than of the HFR pellets. At the same time, the difference between Type A and B pellets is below 10% for each method.

Besides the apparent density, also the volume scaling factors show large differences between the methods. The pellets from the MF are 30% smaller than the ones from the HFR. Since the number of volatiles released will be similar, the porosity is also expected to be much lower for pellets from the MF.

Comparing the values for pellets devolatilized in the HFR and the FBR shows only smaller differences. In general, the data indicate that the differences depend on the difference in heat flux, as the difference between MF and the LFR is low (Type C) but the difference between MF and FBR pellets is high (Type A or Type B). This agrees with the expectation

since a higher heating range leads to a more rapid volatile release and hence changes the remaining structure. We will discuss the differences between the different pellets further in the next sections.

Table 3 shows also the trend that pellets devolatilized in the MF have stronger shrinkage in radial direction. Pellets devolatilized in the FBR or HFR do not show such a trend. In contrast, for Type C pellets the anisotropy increases slightly for the LFR. However, the accuracy of the measurement does not allow a detailed analysis of this phenomenon. Therefore, it will only be shortly discussed in the analysis of the microCT data.

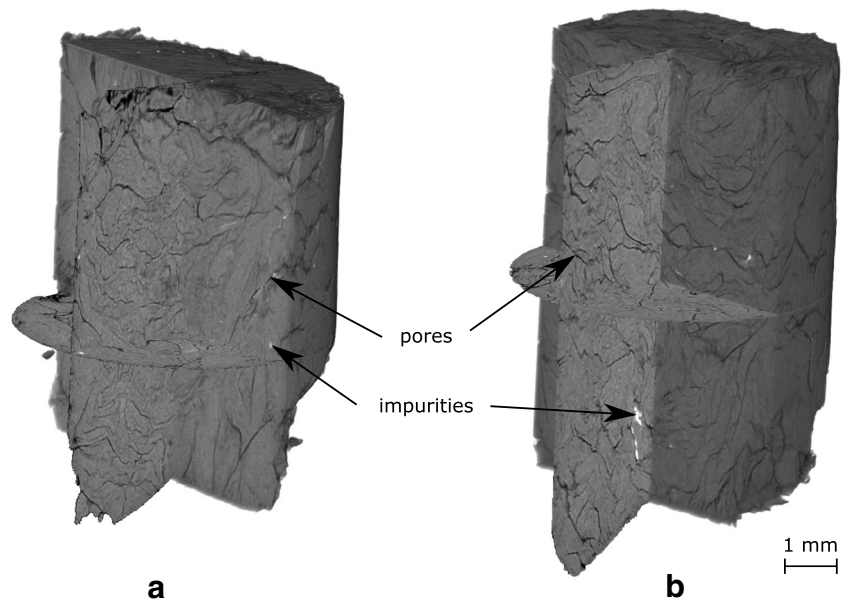
3.1.1 General phenomenological description

In the following, the general change in the pellet structure based on the microCT images is analyzed. As the general behavior of the pellets is expected to be similar, we focused on microCT analysis of the Type A pellets. For Type A pellets different devolatilization methods were applied and will be compared.

Firstly, the raw state of the pellets is considered. The microCT images in Fig. 3 show the initial structure of two raw pellets by displaying the measured linear attenuation coefficient in different grayscales. We see pores and cracks between the wood chips pressed together. As the voxel size of 12 μm is bigger than the typical pore size of the wooden chips [19], they appear as a nearly uniform solid. Figure 3 also reveals some impurities with a much higher density visible as white dots.

An analysis of the raw pellet's pore network shows, that there is mainly one interconnected pore network. The pore network is open, as some pores start as cracks on the surface. The pores show often a U-shape diffracted in the same direction. This morphology results from the pressing during

Fig. 3 Grayscale 3D images of the linear attenuation coefficient for the raw Type A pellets measured with the microCT. In the front, cross-cuts are shown and in the back a volumetric rendering. **a** Before devolatilization in MF. **b** Before devolatilization FBR

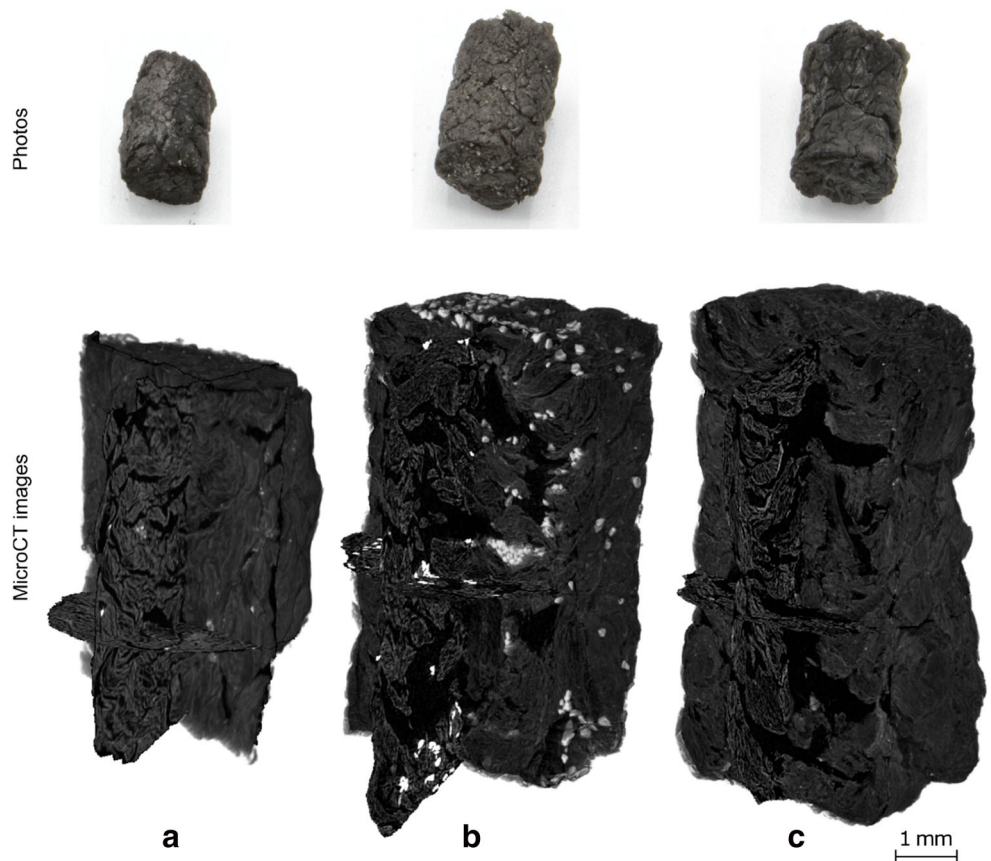


production diffracting the U-shape in the opposite direction of the pressing.

Figure 4 shows the same pellets from Fig. 3 in an equal orientation after the devolatilization. The pellet devolatilized in the HFR will be discussed later. Since the

same grayscale range is used as for the raw pellets, the pellets appear much darker. In the case of the pellet from the FBR, also big white particles are now visible, which are quartz sand. The sand particles can be found on the surface as well as inside the pellet. Their influence will be

Fig. 4 Photos of the devolatilized Type A pellets as well as grayscale 3D images of the linear attenuation coefficient measured with microCT. In the front of the computed tomography images, cross-cuts are shown and in the back the attenuation coefficient is rendered volumetrically. **a** Devolatilization in MF. **b** Devolatilization in FBR. **c** Devolatilization in HFR



discussed further when comparing to the image of the pellet devolatilized in the HFR.

The figure illustrates that the original shape of the pellets is preserved during devolatilization for both methods. The cylindrical shape and the ground surfaces are visible. The volume of the body-fitted surface is only 20% smaller than the volume of an enveloping perfect cylinder for the FBR pellet and 16% smaller for the MF pellet (see Section 2 for the definition of the body-fitted surface). The microCT images also illustrate again the different shrinkage in the radial direction. Note that the axial length of the pellets is different due to manufacturing.

For both pellets, we see a massive increase in the amount and size of the pores. Despite the visible different pore volume and shrinkage, some similarities in the internal structure are visible. These similarities we want to discuss

first to give a general overview. Firstly, it is striking that the biggest pores exist in the pellet's inner part, and they are not at the surface or directly connected to the outer surface. By contrast, the pores directly at the boundary are often relatively small. From the outside, only small cracks are visible, as also shown in the photos in Fig. 4.

To get a deep insight into how the structure of the devolatilized pellets relates to the raw pellet structure, Fig. 5 shows an upscaled image of the devolatilized pellet as a projection on the initial pellet in green. For this upscaling, an image registration algorithm is used to calculate the transformation. The process is described in Section 2. Looking at the boundary and the inclusions, one can see that the microstructures of the raw and devolatilized pellets are similar. Of course, discrepancies exist. They result from the conversion process and possibly also from small breakages

Fig. 5 Axial and radial cross-cuts through the linear attenuation coefficient measured with the microCT. In gray, the values of the raw Type A pellets are shown, and in green, the values of the same pellet in the devolatilized state are shown with upscaled dimensions.
a Devolatilization in MF.
b Devolatilization in FBR

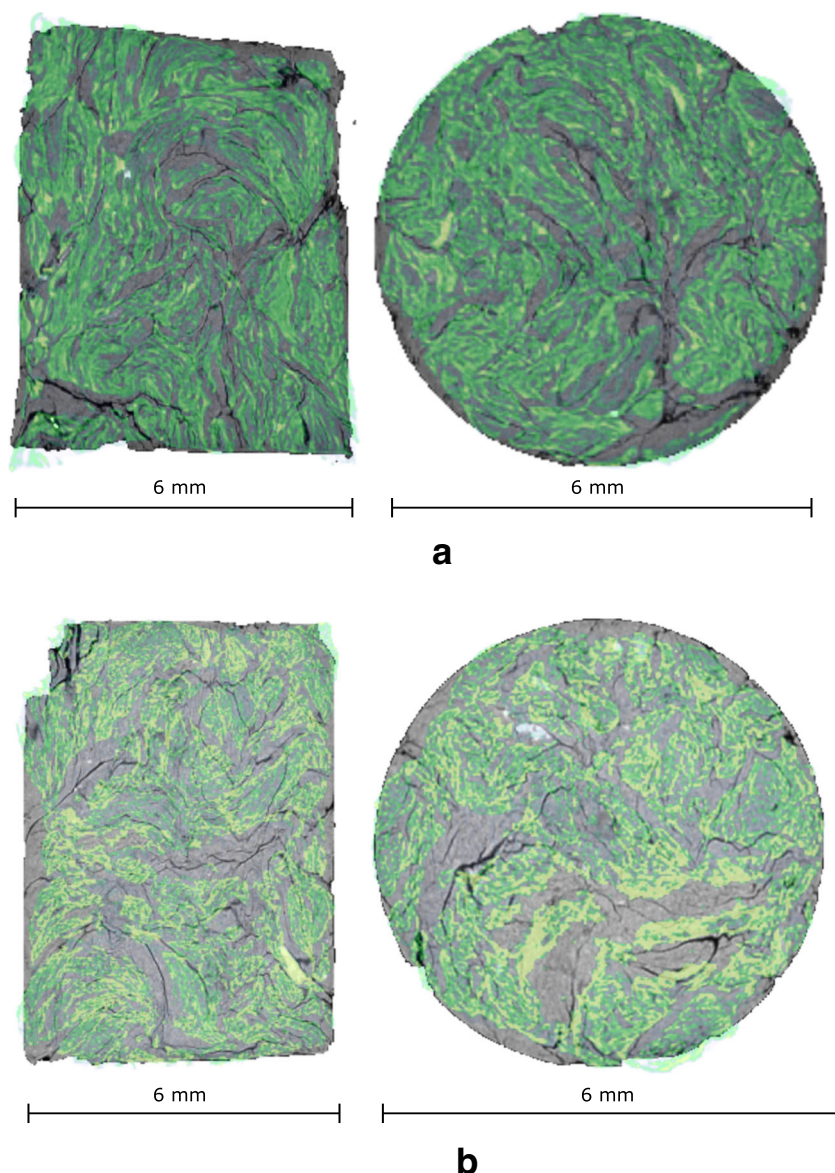
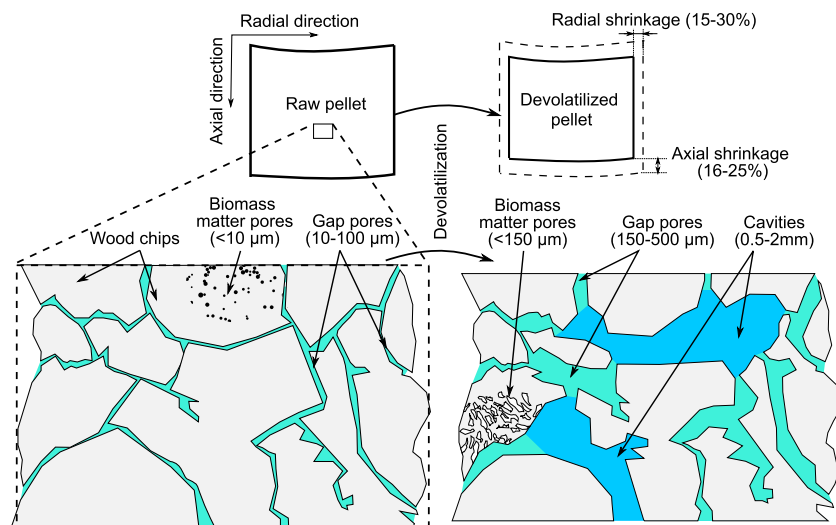


Fig. 6 Schematic representation of microstructural modification occurring in the wood pellet during devolatilization based on the microCT analysis. The scales of the pores are based on chord lengths and the shrinkage factors are based on Table 3



or uneven shrinkage. Hence, the matching between the images can only be an approximation and the images do not overlap perfectly. Nevertheless, the figure illustrates that bigger pores in the devolatilized pellet appear in locations where pores already existed in the raw pellet. Previously dense solid-like areas in the image now have many small pores.

In general, we can identify three types of pores after devolatilization which are also shown in Fig. 6:

Gap pores: The major part of the pore network consists of gap pores. They mainly are located in areas where pores already existed in the raw pellet. Hence, they are located in the gaps between the chips and a primary orientation of the pores is caused due to pressing in production. The cross-sectional area of these pores appears to decrease towards the boundary. On the surface, they appear as cracks.

Cavities: In the inside of the pellet the gap pores form large interconnected cavities. In general, the large cavities are not connected directly to the outer surface but only via smaller pores.

Biomass matter pores: These are the relatively small pores which appear in the previously dense appearing solid zones. Although they might appear separate in a two-dimensional cut, almost all of these pores are connected to the global pore network. Despite the fact that they are relatively small their total volume is significant.

3.1.2 Differences between the pellets from the muffle furnace and the fluidized bed

Besides the common basic structure, large discrepancies between the pellet devolatilized in the MF and the FBR are clearly visible. Firstly, it should be noted, that the surface

of the pellet from the muffle is smoother (see Fig. 5). This was already indicated when discussing the volume of the body-fitted surface compared to an ideal cylinder.

The major difference between the two pellets is a much smaller shrinkage and a much higher porosity for the pellet from the FBR. Through the image registration algorithm, the microCT images can also quantify the shrinkage in each dimension. The shrinkage based on the microCT data is based on the scaling factors of the three-dimensional transformation needed to project the raw pellet to the devolatilized pellet. As we are using a cartesian coordinate system for the transformation, two scaling factors exist for the radial component. The values are shown in Table 4. They agree quite well with the values of Table 3 which are based on simple measurements of the length and radius before and after devolatilization. The microCT based shrinkage values also show the trend of anisotropic shrinkage for the pellet from the MF and isotropic shrinkage for the pellet from the FBR. Quantifying the porosity with the given microCT images is in contrast a bit more difficult as pointed out in Section 2. The used analysis results in a porosity of 0.43–0.51 for the MF pellet and 0.55–0.62 for the FBR. The interval describes the range for which the segmentation gives visually reasonable results. The FBR range is very similar to the 0.64 found by [28] for the inner part of

Table 4 Axial and radial scaling factors calculated from the microCT images of the raw and devolatilized Type A pellets

Devol. method	Radial scaling factor [%]	Axial scaling factor [%]
MF	70, 69	75
FBR	85, 85	84

First value for the radial shrinkage is the perpendicular and the second one is in direction of the face normal of the ground surface (see Fig. 5)

a pellet. They studied a microCT of poplar wood pellets in a reactor with airflow at 1000 °C. However, since the voxelsize of 12 μm used in this work is insufficient to resolve all pores inside the biomass matter, the porosity calculated from microCT is expected to underestimate the porosity. For comparison, by using high-pressure mercury porosimetry, [24] measured a porosity of 0.91 for wood chips devolatilized in a fluidized bed. [29] determined the porosity of rice straw pellets devolatilized in a fixed bed to be in the range 0.82–0.9. Thus, the given total values for the porosity in this work show only the amount of large-scale pores and are mainly used for a relative comparison.

3.1.3 Differences between the pellets from the fluidized bed and the high gas flow tube reactor

Between the pellets devolatilized in the FBR and the HFR, no major differences are visible besides the penetration of sand. The radial scaling factor is around 10% higher for the FBR pellets, which is a slightly higher difference than the one measured with the compression tester and the caliper. The porosity of the HFR pellet is in the range of 0.54–0.59, hence very similar to the 0.55–0.62 of the FBR pellets.

To better assess the similarity between the FBR and HFR a descriptive quantity is needed. Due to the pores' complex three-dimensional shape, a separation into individual pores is not possible, and hence no distinct pore sizes exist. Instead, we are using chord lengths in three directions for describing the pore size and shape. Note that we assumed

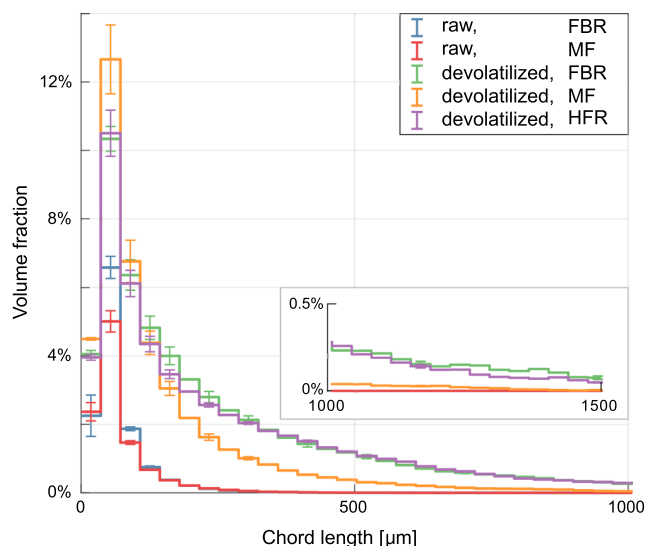


Fig. 7 Histogram of the pores chord length distributions of Type A pellets obtained from the micro CT images. Chords are straight lines that start and end at the pore boundary. A chord spacing of one pixel is used to cover the entire pore network. The y-axis shows the volume fraction occupied by chords with the given length. See Section 2 for the details about the volume fraction calculation. The error bars indicate the uncertainty from the manual binarization

the volume occupied by sand particles to be part of the pore volume. The calculated chord length distributions are shown in Fig. 7 with the volume fraction on the y-axis. The volume fraction is based on the entire pellets' volume. Hence, the sum of all bins is equal to the porosity. The details about the calculation of the volume fraction and the cord lengths were explained in Section 2.

Comparing the distribution before and after the devolatilization shows that distribution gets broader and higher. Hence, there is an increase in the number of small pores. At the same time pores with larger dimensions emerge. In the comparison of the images, we saw that large pores mainly emerge from the small pores already existing in the raw state. The introduced classification of pores, illustrated in Fig. 6, is not visible as separate peaks in the chord length distribution since the pore network is interconnected and no sharp separation in pore sizes exists. Furthermore, the typical size of a pore type depends on the devolatilization methods. For the biomass matter pores one can nevertheless give a typical chord length range, which corresponds to the first peak, i.e., a chord length between 0 and 150 micrometers. However, the major purpose of this plot is to allow assessing the differences between the different devolatilization methods. One can clearly see that there is very good agreement between the pore structure of the pellet from the FBR and the HFR. In contrast, the pellet from the MF shows a much narrower distribution. Hence, the pellet from the muffle has more biomass matter pores and less and smaller large-scale pores. This agrees well with the visual perception (see Fig. 7). However, especially the smallest biomass matter pores are not well resolved by the used microCT data and, therefore, the sensitivity to small changes in the segmentation is high. Nevertheless, for larger chords, the variation becomes smaller and shows that the pore structure of the FBR and the HFR pellet are also quantitatively similar. Hence, despite the quartz sand particles having enough space for oscillations in internal cavities, no significant abrasion of the internal structure can be measured from the microCT data for the used reactor conditions and residence time.

3.1.4 Bed material penetration

One key difference between the pellet devolatilized in the FBR and the HFR is the penetration of the bed material into the pellet. However, since the chord length distribution of the pore sizes is very similar for both reactor types, we assume that the sand does not significantly change the pore structure. Nevertheless, the added mass might influence the fluidization behavior. Therefore, we estimated the mass of the sand with two methods. For the first estimation, we can quantify the sand's volume from the microCT images and use the density of the inert sand. The sand volume

fraction is about 3 to 5%, and consequently, the mass fraction is between 20 and 35%. The volume fraction of sand illustrated in Fig. 4 is, for example, 3%.

For counterchecking the results, a second estimation was calculated. For this purpose, we assumed that the density of the pellets devolatilized in the FBR and the HFR are equal. This assumption is based on the expected similar values for the remaining mass and the observation that the outer volume and the pore structure are very similar. By simply subtracting the average masses of pellets of the same initial size after devolatilization, the mass of sand can be estimated. Note that the apparent volume of the FBR pellets is also slightly bigger, and hence, the apparent density is nearly equal, as shown in Table 3. The resulting fraction of sand is about 15% in the median. Comparing the 25th percentile of the HFR pellet's masses and the 75th percentile of the FBR pellet's masses gives an upper value for the fraction of around 30%. Thus, both estimates for the mass fraction are in a similar range. Hence, we conclude that the median of the sand's mass fraction appears to have an order of magnitude of 15 to 30%. If the char is only 70% of the final mass, the sand increases the pellet's mass by 45% in relation to the biomass fraction. Therefore, the penetration of sand possibly increases the mass of the devolatilized pellets typically up to 45%.

3.2 Mechanical characterization

In the last section the general structural change of the pellets caused by devolatilization was described. The char pellets were found to be a highly porous structure with a wide range of pore sizes. It was shown that the method of devolatilization has a major influence on the structure. In the following, the pellets will be characterized mechanically and the influence of the method of devolatilization will be investigated further.

3.2.1 Quasi-static compression

For quantifying the degradation of the strength due to the devolatilization, quasi-static uni-axial compression tests are conducted. The detailed procedure is explained in Section 2. Figure 8 shows an excerpt of the measured force-displacement curves of the compression tests. With those examples, we want to discuss the general behavior and the characteristic parameters we are using.

A typical phenomenon for all devolatilization conditions is the existence of microfractures. However, the degree and strength depend on the specific condition. For the pellets from the MF, only a few and small breakages exist before a complete failure of the structure is visible. The complete failure is often identifiable by a sudden drop in the measured force or the curve's flattening with the appearance

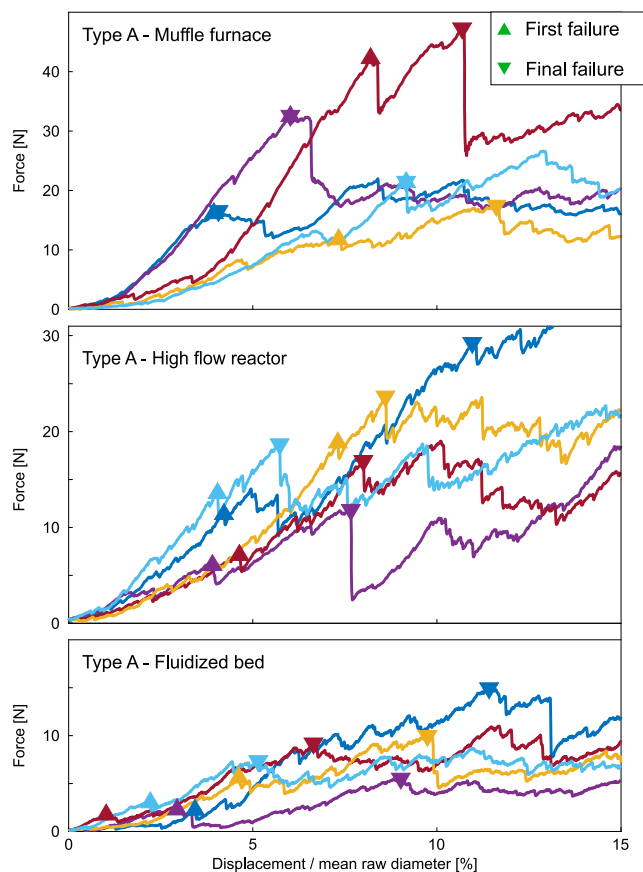


Fig. 8 Excerpt of measured force-displacement curves. The displacement is normalized by the mean raw diameter (Table 1). For each displayed condition five measurements were randomly picked

of high-frequency changes. These high-frequency changes are probably caused by collapsing pores and moving chips. After failure, the loose bulk of devolatilized chips was still stable under compression, and, therefore, the measured force could further increase. For the pellets from the HFR or FBR, the behavior is slightly different. The high-frequency changes in the measured force exist often from the beginning. Furthermore, bigger dips in the measured force exist even when the structure appears to be still stable. The point of complete failure is not always clearly identifiable. For some cases, a plastic failure is visible with high-frequency fluctuations due to moving chips. In other cases, multiple abrupt drops are visible.

In principle, the different behavior fits well with the results of microCT image analysis, since the HFR and FBR pellets showed a much higher porosity with a more loosely connected char structure compared to the MF pellets. Hence, more regions with highly weakened bonds exist which can break under low loads and lead to high-frequency fluctuations. Also, more cavities, which can collapse, exist. Furthermore, the increased porosity can result in more movement after the breakage.

Due to the described behavior, two quantities are analyzed to characterize the pellets' strength. Firstly, the point where the first micro failure with a measured force drop of around 1 N or 20% occurs, called the first failure, is used. Typically, the first fragments can be found after this point. Secondly, the complete failure point is estimated. We are using the point where either the measured force drops strongly or the curve flattens significantly. The used points are visualized in Fig. 8 for the given force-displacement curves. With the final failure point, we want to approximate the force needed to destroy the pellet's structure. However, uncertainties exist as it is not always apparent from the force-displacement curve when this point is reached. Also, the definition is not entirely strict, as parts can break apart which still consist of multiple chips in a porous structure.

All resulting values are shown in Fig. 9. From the figure, it becomes clear that the used quantities fluctuate strongly. The fluctuations are likely caused by deviations already existing in the raw condition and the devolatilization process but also by the determination of the breakage points itself. Nevertheless, some trends are still visible. Firstly, one can note that the different strengths in raw condition persist and results in different strengths after devolatilization. Therefore, the used type-dependent normalization is applied to allow the comparison between different wood pellet types. Compared to the raw strength, the first failure already occurs at very low energies of down to 0.1 J/kg. For Type A pellets from the MF, the first failure and final failure points are nearly equal, which indicates their compact and stable structure. For Type B and C pellets from the MF first failure at lower forces occurs more often.

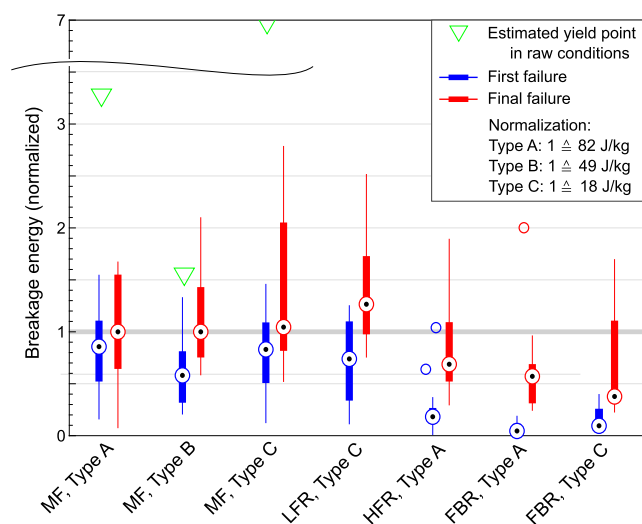


Fig. 9 Boxplot of breakage energies for the first failure and final failure. Values normalized to the first failure at MF conditions for each type. Estimated yield point in raw conditions for comparison (see Section 2)

Despite the different absolute values for Type A and C pellets, the relative decrease of the breakage energy at first failure between MF and FBR pellets is similar. The LFR devolatilization for the Type C pellets seems to result in similarly strong pellets for the MF method. In contrast, the Type A pellets from the HFR are more similar to the FBR pellets. The dependency on the method is expected to result from the different pore structures and, therefore, from the different heat flux. The pellets from the highest heat flux method, the FBR devolatilization, are the weakest. However, the pellets from a fluidized bed are also pre-stressed due to contacts with walls and the bed material which could reduce the strength additionally. Nevertheless, due to the high deviations in the pore structure, we expect the pore structure to have the crucial influence.

For the final failure, the described tendency of lower breakage energies for higher heat flux methods is less strong since the final failure occurs later and the values scatter more. The Type A pellets from the HFR show only slightly lower energies for the final failure compared to the MF conditions. For Type C pellets from the LFR, the median of the final failure breakage energy is even slightly higher compared to the MF. This is expected to be a measurement error due to the large scattering. Nevertheless, the general trend in the decreasing breakage energy seems to be still visible for the final failure.

In general, the quasi-static loading showed that the devolatilized wood pellets are a fragile though stable structure which breakage behavior is mainly characterized by collapsing pores. Thus, the method of devolatilization is significant as it influences the pore structure. However, the difference in strength seems to decrease for higher heat fluxes, as the strength of FBR pellets is only slightly reduced compared to the HFR. For all cases, minimal forces might be needed to lead to first fragmentation.

3.2.2 Impact tests

In the following section, the dynamic impact resistance of the devolatilized pellets will be analyzed. Dynamic impact is a typical load for a pellet inside a fluidized bed reactor and is, therefore, discussed in the work at hand. As explained in Section 2, drop tests on a hard surface are used to study an isolated impact.

Since our pre-tests (Section 2) showed large fluctuation and the high amount impacts needed before breakage, we focused mainly on studying one type of pellets. Pellets of Type A devolatilized in the HFR were chosen as an example. As shown in the previous sections, they are mechanically similar to the pellets from the FBR but the mechanical stress of a fluidized bed and the mass fluctuations caused by penetrating bed material is avoided. 100 consecutive impacts

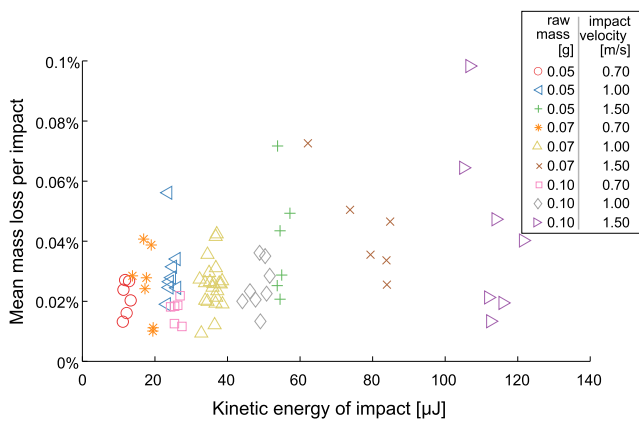


Fig. 10 Mean mass loss per impact plotted versus the kinetic energy at contact. The average is calculated for each pellet over all impacts. Three different velocities and three differently long Type A pellets were used. The different markers in the plot indicate the different configurations

of 75 samples at different conditions were conducted. The drop height, as well as the pellet length and, thus, the mass, was varied.

In general, the consecutive impacts have two effects: The creation of fines due to micro fragmentation and the pellet’s breakage. At first, we will look at the resulting average mass loss without breakage plotted versus the kinetic energy of a single impact in Fig. 10. Although the scattering is strong, the figure shows that the mass loss increases, as expected, with increasing impact energy. Higher impact energies will result in higher stress which can lead to more bond failures. Typically, around 2–3% of the mass is lost as fines after 100 impacts. The scattering appears to increase with increasing kinetic energies. This could be explained by the increased randomness of the impact due to a longer travel length. Also, the pellet structure becomes more important, as the pore structure will influence the size of the fragments breaking apart by impact.

Additionally, Fig. 10 shows that a higher pellet length itself does not significantly increase the mass loss. A strong dependence on the length alone would result in groups of values not following the general trend. Due to the strong scattering and small range of impact energies, no universal trend can be deduced.

Besides the constant mass loss by micro fragmentation, a complete breakage can occur. In such a case, it was found that mainly two pieces exist after breakage. Also, some fines are created amounting on average to around 0.2% of the mass before breakage. The number of broken pellets is shown in Fig. 11 for different maximally considered kinetic energies. As expected, the breakage probability increases with the number of impacts and with higher kinetic energies at contact. In general, the increase seems to be roughly linear. However, the graph for the low kinetic

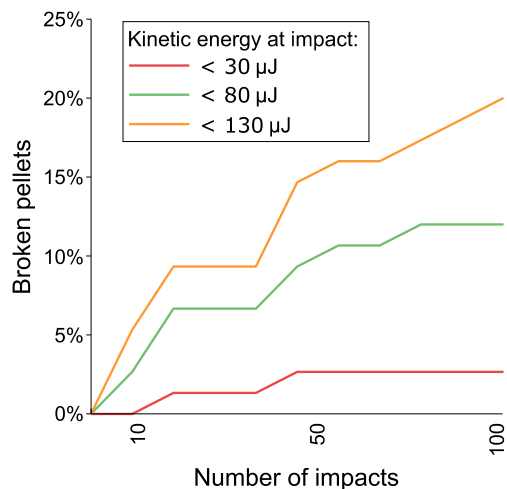


Fig. 11 Number of broken pellets during impact test as a line plot. The different lines show the values for all impacts with a kinetic energy lower than a given value

energy indicates that there might be a maximum value of the breakage probability. Plotting the mass loss also per impact in Fig. 12 supports the assumption since the mass loss per impact also reduces with an increasing amount of impacts. This indicates that the number of bonds breaking under given kinetic energy at impact reduces, and a more stable core of the pellet remains.

To verify that the results transfer to other types of pellets, pellets of Type B from the HFR were also tested but only with one specific kinetic energy at impact. Figure 13 shows that the median values follow the general trend of a decreasing mass loss for a larger number of impacts. However, significantly more outliers with larger mass loss exist. This agrees with the compression test results where the energy required for the first failure for Type B pellets was also much lower and the standard deviation higher. Thus, the structure of devolatilized Type B pellets is likely more fragile leading to larger fragments breaking apart.

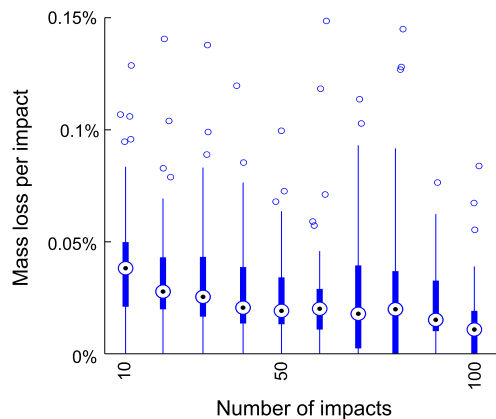


Fig. 12 Box plot of the mass loss per impact. The mass loss is given in percent of the initial mass after devolatilization

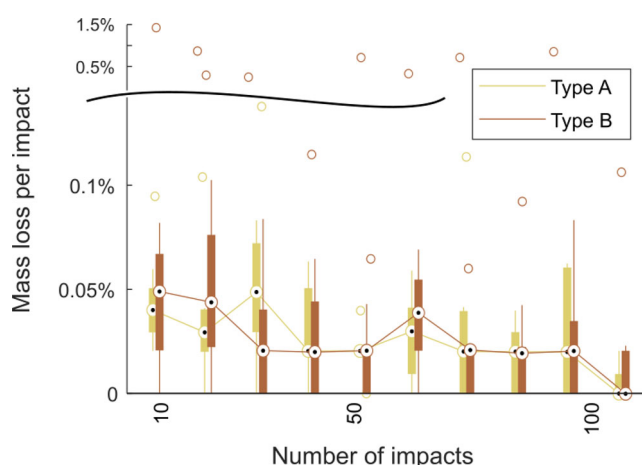


Fig. 13 Box plot of mass loss per impact of Type A and Type C pellets for a kinetic energy at the impact of about $25 \mu\text{J}$ (corresponds to a pellet length of 10 mm and 1.5 m/s at impact)

3.2.3 Primary fragmentation during devolatilization

For biomass particles, significantly primary fragmentation during devolatilization occurs in a fluidized bed [1]. However, for pellets, primary fragmentation seemed to occur less frequently. The breakage probability from our experiments for differently long pellets of Type A during devolatilization is shown in Table 5. We also included the breakage probability for pellets from the HFR devolatilization. For pellets from the MF no primary fragmentation occurred.

Table 5 shows that breakage probability is higher for pellets from the FBR. Since the structure of the pellets after devolatilization and their strength is rather similar, for a first approximation one can assume that the influence of the increased heat flux is neglectable and the increased breakage results from the additional mechanical stress in the bed. Mechanical stresses include pellet-wall and pellet-bed interactions. Based on this assumption one can estimate that for a typical length distribution of the Type A pellets, at least roughly 50% of the breakage in a bubbling fluidized bed reactor is resulting from the additional mechanical stresses. Nevertheless, also the breakage in the HFR can result from external mechanical stress since the impact test

Table 5 Number of broken pellets shown as breakage probability during devolatilization for Type A pellets

Pellet length [mm]	Breakage probability	Breakage probability	Breakage probability
	FBR	HFR	MF
10	10%	0%	0%
15	–	16%	0%
20	50%	30%	0%

showed that small kinetic energies might result in breakage. The increased probability for longer and, hence, heavier pellets could also indicate a dependency on the increased kinetic energy of the heavier pellets. However, also the devolatilization process itself could be influenced by the increased length and causing this dependency since the mass per surface area is increasing. Thus, more gas must be released through the pore network. Hence, the stress due to overpressure could be increased. Another possible cause could be that a longer pellet will have more imperfections and the chance of areas with only a few bonds will be increased. We also found that the pellet broke nearly always into two identifiable and cylindrical segments in the reactor. Hence, a burst of the entire pellet due to overpressure is unlikely.

4 Conclusion

Gasification of biomass is a promising approach for an environmentally friendly generation of synthesis gas from biomass. The conversion of pelletized biomass in fluidized bed reactors is especially interesting for this application due to the better fuel properties of pellets and the efficient mixing of fluidized beds. With a focus on this application, the work at hand analyzed the changes caused by devolatilization on the properties and microstructure of wood pellets. The goal was to get more insights into the conversion process and possible impacts on a reactor.

Devolatilization of the examined wood pellets resulted in a macro-porous char pellet. The existing pore network in raw conditions between the wooden chips is substantially enlarged, forming an interconnected network of pores and cavities. The porous structure caused by the devolatilization is also characterizing the breakage behavior. Small micro fragmentations are typical during uni-axial, quasi-static compression and indicate the continuous failure of bonds and pores collapsing. The failure behavior of the entire pellet's structure is divers due to the dependency on the pore structure. Low kinetic energy impacts can already lead to fragmentation and the creation of fines. Continuous impacts increase the breakage probability, but the mass loss by micro fragments gradually reduces.

Comparing the influence of the different processes used for devolatilization showed a strong dependence. A higher heat flux seems to lead to a more porous and hence weaker structure. However, only small differences were found comparing pellets from a fluidized bed reactor (FBR) and the same reactor without bed but with an equally high gas flow (HFR). The similarity of the pellets from the fluidized bed and the high flow reactor allows further conclusions: In the FBR, bed material can enter the pore network and increase the pellets' mass up to 45%. However,

the influence on the internal structure and the mechanical behavior was neglectable. Comparing the probability of primary fragmentation of the wood pellets inside both reactors indicates that at least half of the breakage in the FBR results from external mechanical stresses.

Due to the bed material penetrating the pellets, mixing could be increased because of the hot bed material entering the inside of the pellet. Especially in the case of an oxygen carrier or a sorbent as bed material, an increased reactivity inside the pellet is possible. However, further research is needed to understand these influences. For the mechanics of a devolatilized wood pellet, the work at hand showed that the pore structure could not be neglected. However, further studies are needed to quantify the attrition by surface wear. Nevertheless, it became clear that the breakage and attrition behavior is influenced strongly by the formation of a large-scale pore network and, therefore, depends on the heat flux during devolatilization.

Acknowledgements We want to thank Hari Haran Velmurugan for his help in this work.

Funding Open Access funding enabled and organized by Projekt DEAL. Funded by the Deutsche Forschungsgemeinschaft (DFG, German Research Foundation) - DO 2026/5-1 and HE 4526/21-1, and National Natural Science Foundation of China (51761135119).

Availability of data and material The used wood pellets are commercially available. All raw data from the mechanical characterization and micro-computed tomography are made available on the research data repository of the Hamburg University of Technology called TORE using doi.org/10.15480/336.3265

Declarations

Conflict of interest The authors declare no competing interests.

Open Access This article is licensed under a Creative Commons Attribution 4.0 International License, which permits use, sharing, adaptation, distribution and reproduction in any medium or format, as long as you give appropriate credit to the original author(s) and the source, provide a link to the Creative Commons licence, and indicate if changes were made. The images or other third party material in this article are included in the article's Creative Commons licence, unless indicated otherwise in a credit line to the material. If material is not included in the article's Creative Commons licence and your intended use is not permitted by statutory regulation or exceeds the permitted use, you will need to obtain permission directly from the copyright holder. To view a copy of this licence, visit <http://creativecommons.org/licenses/by/4.0/>.

References

1. Ammendola P, Chirone R, Ruoppolo G, Scala F (2013) The effect of pelletization on the attrition of wood under fluidized bed combustion and gasification conditions. *Proc Combust Inst* 34(2):2735–2740. <https://doi.org/10.1016/j.proci.2012.06.008>
2. Deutsches Institut für Normung eV (51720:2001-03) Testing of solid fuels: determination of volatile matter content
3. Deutsches Institut für Normung eV (DIN 51734:2008-12) Testing of solid fuels: Proximate analysis and calculation of fixed carbon
4. Frodeson S, Henriksson G, Berghel J (2017) Pelletizing pure biomass substances to investigate the mechanical properties and bonding mechanisms. *BioResources* 13(1). <https://doi.org/10.15376/biores.13.1.1202-1222>
5. Ge H, Guo W, Shen L, Song T, Xiao J (2016) Biomass gasification using chemical looping in a 25 kW th reactor with natural hematite as oxygen carrier. *Chem Eng J* 286:174–183. <https://doi.org/10.1016/j.cej.2015.10.092>
6. Gil J, Corella J, Aznar MP, Caballero MA (1999) Biomass gasification in atmospheric and bubbling fluidized bed: effect of the type of gasifying agent on the product distribution. *Biomass Bioenergy* 17(5):389–403. [https://doi.org/10.1016/S0961-9534\(99\)00055-0](https://doi.org/10.1016/S0961-9534(99)00055-0)
7. Hanchate N, Ramani S, Mathpati CS, Dalvi VH (2021) Biomass gasification using dual fluidized bed gasification systems: a review. *J Clean Prod* 280:123148. <https://doi.org/10.1016/j.jclepro.2020.123148>
8. Haus J, Goltzsche M, Hartge EU, Heinrich S, Werther J (2019) Gasification kinetics of lignite char in a fluidized bed of reactive oxygen carrier particles. *Fuel* 236:166–178. <https://doi.org/10.1016/j.fuel.2018.08.151>
9. Horton SR, Mohr RJ, Zhang Y, Petrocelli FP, Klein MT (2016) Molecular-level kinetic modeling of biomass gasification. *Energy Fuels* 30(3):1647–1661. <https://doi.org/10.1021/acs.energyfuels.5b01988>
10. Kaliyan N, Morey RV (2010) Natural binders and solid bridge type binding mechanisms in briquettes and pellets made from corn stover and switchgrass. *Bioresour Technol* 101(3):1082–1090. <https://doi.org/10.1016/j.biortech.2009.08.064>
11. Kaliyan N, Vance Morey R (2009) Factors affecting strength and durability of densified biomass products. *Biomass Bioenergy* 33(3):337–359. <https://doi.org/10.1016/j.biombioe.2008.08.005>
12. Karamchandani A, Yi H, Puri VM (2016) Comparison and explanation of predictive capability of pellet quality metrics based on fundamental mechanical properties of ground willow and switchgrass. *Adv Powder Technol* 27(4):1411–1417. <https://doi.org/10.1016/j.appt.2016.04.036>
13. Kruggel-Emden H, Sudbrock F, Wirtz S, Scherer V (2012) Experimental and numerical investigation of the bulk behavior of wood pellets on a model type grate. *Granul Matter* 14(6):681–693. <https://doi.org/10.1007/s10035-012-0376-6>
14. Molino A, Chianese S, Musmarra D (2016) Biomass gasification technology: the state of the art overview. *J Energy Chem* 25(1):10–25. <https://doi.org/10.1016/j.jechem.2015.11.005>
15. Oveisi E, Lau A, Sokhansanj S, Lim CJ, Bi X, Larsson SH, Melin S (2013) Breakage behavior of wood pellets due to free fall. *Powder Technol* 235:493–499. <https://doi.org/10.1016/j.powtec.2012.10.022>
16. Paulauskas R, Striugas N, Zakarauskas K, Dziugys A, Vorotinskiene L (2018) Investigation of regularities of pelletized biomass thermal deformations during pyrolysis. *Therm Sci* 22(1 Part B):603–612. <https://doi.org/10.2298/TSCI160916090P>
17. Peng JH, Bi HT, Sokhansanj S, Lim JC, Melin S (2010) An economical and market analysis of Canadian wood pellets. *Int J Green Energy* 7(2):128–142. <https://doi.org/10.1080/15435071003673518>
18. Pfeifer C, Puchner B, Hofbauer H (2009) Comparison of dual fluidized bed steam gasification of biomass with and without selective transport of CO₂. *Chem Eng Sci* 64(23):5073–5083. <https://doi.org/10.1016/j.ces.2009.08.014>
19. Plötze M, Niemz P (2011) Porosity and pore size distribution of different wood types as determined by mercury intrusion porosimetry. *Eur J Wood Wood Prod* 69(4):649–657. <https://doi.org/10.1007/s00107-010-0504-0>

20. Rostrup-Nielsen JR, Sehested J, JK Nørskov (2002) Hydrogen and synthesis gas by steam- and CO₂ reforming. *Adv Catal* 47:65–139. [https://doi.org/10.1016/S0360-0564\(02\)47006-X](https://doi.org/10.1016/S0360-0564(02)47006-X)
21. Rumpf H (1962) The strength of granules and agglomerates. *Agglomeration* 379–413
22. Scala F, Chirone R, Salatino P (2013) Attrition phenomena relevant to fluidized bed combustion and gasification systems. Elsevier. <https://doi.org/10.1533/9780857098801.1.254>
23. Schmid JC, Pröll T, Kitzler H, Pfeifer C, Hofbauer H (2012) Cold flow model investigations of the countercurrent flow of a dual circulating fluidized bed gasifier. *Biomass Convers Biorefinery* 2(3):229–244. <https://doi.org/10.1007/s13399-012-0035-5>
24. Senneca O (2007) Kinetics of pyrolysis, combustion and gasification of three biomass fuels. *Fuel Process Technol* 88(1):87–97. <https://doi.org/10.1016/j.fuproc.2006.09.002>
25. Siyal AA, Liu Y, Mao X, Ali B, Husaain S, Dai J, Zhang T, Fu J, Liu G (2021) Characterization and quality analysis of wood pellets: effect of pelletization and torrefaction process variables on quality of pellets. *Biomass Convers Biorefinery* <https://doi.org/10.1007/s13399-020-01235-6>
26. Stelte W, Holm JK, Sanadi AR, Barsberg S, Ahrenfeldt J, Henriksen UB (2011) A study of bonding and failure mechanisms in fuel pellets from different biomass resources. *Biomass Bioenergy* 35(2):910–918. <https://doi.org/10.1016/j.biombioe.2010.11.003>
27. Stelte W, Sanadi AR, Shang L, Holm JK, Ahrenfeldt J, Henriksen UB (2012) Recent developments in biomass pelletization—a review. *BioResources* 7(3):4451–4490. <https://doi.org/10.15376/biores.7.3.4451-4490>
28. Strandberg A, Thyrel M, Skoglund N, Lestander TA, Broström M, Backman R (2018) Biomass pellet combustion: Cavities and ash formation characterized by synchrotron X-ray micro-tomography. *Fuel Process Technol* 176:211–220. <https://doi.org/10.1016/j.fuproc.2018.03.023>
29. Wang T, Meng D, Zhu J, Chen X (2020) Effects of pelletizing conditions on the structure of rice straw-pellet pyrolysis char. *Fuel* 264:116909. <https://doi.org/10.1016/j.fuel.2019.116909>
30. Wen CY, Yu YH (1966) A generalized method for predicting the minimum fluidization velocity. *AIChE J* 12(3):610–612. <https://doi.org/10.1002/aic.690120343>
31. Werther J, Reppenhagen J (1999) Catalyst attrition in fluidized-bed systems. *AIChE J* 45(9):2001–2010. <https://doi.org/10.1002/aic.690450916>
32. Whittaker C, Shield I (2017) Factors affecting wood, energy grass and straw pellet durability—a review. *Renew Sustain Energy Rev* 71:1–11. <https://doi.org/10.1016/j.rser.2016.12.119>
33. Williams O, Taylor S, Lester E, Kingman S, Giddings D, Eastwick C (2018) Applicability of mechanical tests for biomass pellet characterisation for bioenergy applications. *Materials* 11(8). <https://doi.org/10.3390/ma11081329>
34. Wyrwat T, Yazdanpanah M, Heinrich S (2020) Bubble properties in bubbling and turbulent fluidized beds for particles of Geldart's group B. *Processes* 8(9):1098. <https://doi.org/10.3390/pr8091098>
35. Yin S, Shen L, Dosta M, Hartge EU, Heinrich S, Lu P, Werther J, Song T (2018) Chemical looping gasification of a biomass pellet with a manganese ore as an oxygen carrier in the fluidized bed. *Energy Fuels* 32(11):11674–11682. <https://doi.org/10.1021/acs.energyfuels.8b02849>
36. Zhang L, Qi S, Ma L, Guo S, Li Z, Li G, Yang J, Zou Y, Li T, Hou X (2020) Three-dimensional pore characterization of intact loess and compacted loess with micron scale computed tomography and mercury intrusion porosimetry. *Sci Rep* 10(1):8511. <https://doi.org/10.1038/s41598-020-65302-8>

Publisher's Note Springer Nature remains neutral with regard to jurisdictional claims in published maps and institutional affiliations.